Session 3P7
Modeling and Inverse Problems

Modeling of EBG Structures Using the Transmission Matrix Method
K. Bharath (Georgia Institute of Technology, USA); E. Engin (Georgia Institute of Technology, USA); T. Yoshitaka (Georgia Institute of Technology, USA); M. Swaminathan (Georgia Institute of Technology, USA); 986

Bloch Mode Modelling of the Scattering of Plane Waves and Fano Resonances for a Photonic Crystal Slab
L. C. Botten (University of Technology, Australia); M. A. Byrne (University of Technology, Australia); A. A. Asatryan (University of Technology, Australia); N. A. Nicorovici (University of Technology, Australia); R. C. McPhedran (University of Sydney, Australia); 987

Methods for Mitigating the Effect of Split Reference Planes on High Speed Digital System Interfaces
H. Pan (Intel Corporation, USA); H.-Y. Chao (National Chiao Tung University, Taiwan); C. Pan (Intel Corporation, USA); 988

Multipath Reduction of GPS Measures through Heuristic Techniques of Compensation
V. Barrile (University "Mediterranea" of Reggio Calabria, Italy); M. Cacciola (University "Mediterranea" of Reggio Calabria, Italy); F. Cotroneo (University "Mediterranea" of Reggio Calabria, Italy); 989

Accurate Analysis of Practical Diffraction Gratings
H. A. Kalhor (State University of New York, USA); M. R. Zunoubi (State University of New York, USA); 994

Spectrum Properties of Partially Coherent Modified Bessel-Gauss Beams by a Lens with Aperture
X. R. Lin (Fuzhou University, China); Q. S. Wang (FuJian Dragon Enterprises Co., Ltd, China); C. Y. Peng (Putian University, China); 995

Generalized Lorenz-Mie Theory for the Arbitrarily Oriented Shaped Beam Scattering by a Spheroid
F. Xu (University of Shanghai for Science and Technology, China); K. F. Ren (Universitéet INSA de Rouen, France); X. S. Cai (University of Shanghai for Science and Technology, China); 996

The Radiated Emission Approach to Specific Emitter Identification
J. Dudczyk (Military University of Technology, Poland); M. Wnuk (Military University of Technology, Poland); 997

Backscattering from Rectangular Plates Illuminated at Grazing Incidence
R. A. Ross (17A Phillips Drive, Westford, MA, 01886, USA); 998

Optimized Satellite System-like Data Fitting on a Spherical Shell
J. Sanchez-Mondragon (Instituto Nacional de Astrofísica, Óptica y Electrónica (INAOE), Mexico); B. Wolf (UNAM, Mexico); M. Tecpoyotl-Torres (Universidad Autónoma del Estado de Morelos, Mexico); J. Escobedo-Alatorre (Universidad Autónoma del Estado de Morelos, Mexico); M. Torres-Cisneros (FIMEEE, México); 999

Modeling of EBG Structures Using the Transmission Matrix Method

K. Bharath, **E. Engin**, **T. Yoshitaka**, **and M. Swaminathan**
Georgia Institute of Technology, USA

Electromagnetic Band Gap (EBG) structures have been employed in noise suppression schemes for mixed signal applications [1]. The design and modeling of these structures typically requires the use of full-wave solvers to characterize their frequency response. However, this can be computationally expensive. In order to reduce the analysis time, the use of a model based simulation tool such as the Transmission Matrix Method (TMM) [2] has been suggested. TMM subsections a given structure into square 'unit cells' and develops an equivalent RLGC netlist. Modeling large plane like structures using this technique has been shown to be very accurate. However, for structures such as the Alternating Impedance (AI) EBG, it was found that simulation results from TMM showed discrepancies from measurement. This was attributed to the Fringe and Gap effects. Thus, accurate simulation of the AI EBG requires the inclusion of these effects into TMM.

The fringe effect can be modeled by adding a fringe capacitor, C_f, and a fringe inductance, L_f, to unit cells that lie along an edge. The fringe elements, C_f and L_f, are calculated by employing empirical formulas for microstrip structures. The Gap effect is modeled as a gap capacitance, Cg, which is added to nodes that lie on either side of an edge. Cg is extracted from the 2D field solver Ansoft Maxwell.

The model to hardware correlation, with and without inclusion of Fringe and Gap Capacitance is shown in Fig. 1. It is seen that the inclusion of Fringe and Gap effects leads to accurate prediction of bandwidth and isolation levels.

The fringe effect is especially pronounced when there are narrow connections between two plane patches. The gap effect becomes important as two separated patches get closer. Hence, both these effects become important to analyze an EBG structure. With a simple extension of TMM to include fringe and gap effects, such complicated structures can be analyzed very efficiently and accurately.

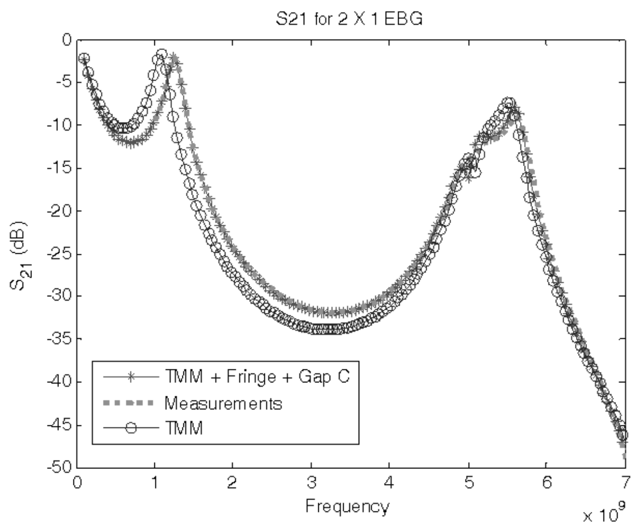

Figure 1: Model to hardware correlation.

REFERENCES

1. Choi, J., V. Govind, and M. Swaminathan, "A novel electromagnetic bandgap (EBG) structure for mixed-signal system applications," *Proc. of IEEE Radio and Wireless Conference*, 243–246, September 2004.
2. Kim, J.-H. and M. Swaminathan, "Modeling of irregular shaped power distribution planes using transmission matrix method," *IEEE Trans. on Adv. Packag.*, Vol. 24, 334–346, August 2001.

Bloch Mode Modelling of the Scattering of Plane Waves and Fano Resonances for a Photonic Crystal Slab

L. C. Botten, **M. A. Byrne**, **A. A. Asatryan**, **and N. A. Nicorovici**
University of Technology, Australia

R. C. Mcphedran
University of Sydney, Australia

Photonic crystals (PC) are amongst the most active research topics in contemporary photonics, with PC slabs prominent amongst the range of structures that are under investigation. In these, the confinement of light occurs via two mechanisms—two-dimensional band gap confinement in the transverse direction, and total internal reflection vertically.

Our interest in these structures arises from the recent observation that Fano resonances, originally discovered in the field of particle physics, are observable in photonic systems. Recent work by Fan, which involved FDTD simulation and a phenomenological approximation of the scattering matrix, showed that the transmission spectrum of the slab could be constructed from a sequence of Lorentzian resonances (with poles in the complex frequency plane) superimposed on the transmittance curve of the unpatterned slab, which acts as a Fabry-Perot (FP) interferometer.

In this paper, we outline a new formulation for the diffraction of a plane wave by a PC slab and show how we may discover the origin of the Fano resonances directly from the the modes of the structure. The technique, based on a multipole-scattering matrix formulation and closely mirroring the geometry of the structure leads to a countably infinite set of modes with propagation constants β_j in the direction of the axis of the cylinders. Only a finite number are propagating (i.e., with β_j real), while the remainder are evanescent and attenuate as they propagate through the slab. We characterize the diffraction at each of the upper and lower planar interfaces of the structure using matrix generalizations of Fresnel "coefficients". Four such matrices are required: T_{12} and R_{12} which are respectively the transmission and reflection matrices for plane wave incidence from air onto a photonic crystal slab of semi-infinite thickness, and T_{21} and R_{21} which are the corresponding matrices for modes incident in the direction of free space from within the slab. These Fresnel matrices closely resemble their familiar scalar forms with, for example, $R_{21} = (Z_2 + J^H Z_1 J)^{-1}(Z_2 - J^H Z_1 J)$. In this expression, Z_1 and Z_2 are respectively the (diagonal) impedance matrices for the free space and slab Bloch modes, with $J^H Z_1 J$ representing the impedance of free space as "seen" by the PC modes.

Finally, we compute the reflection and transmission ($\boldsymbol{T}$) matrices for the PC slab, from which the reflectance and transmittance is calculated. Here, $\boldsymbol{T} = \boldsymbol{T}_{21}\ \boldsymbol{P}(\boldsymbol{I} - \boldsymbol{R}_{21}\boldsymbol{P}\mathrm{R}_{21}\mathrm{P})^{-1}\boldsymbol{T}_{12}$ (where $\boldsymbol{P} = \mathrm{diag}e^{\beta_j h}$), which closely resembles the Airy formulae for a FP interferometer. The symmetric and anti-symmetric slab modes derive from the solutions of $\det(\boldsymbol{I} \mp \boldsymbol{R}_{21}\boldsymbol{P}) = 0$, the solutions of which lie in the complex plane since the modes are lossy. Finally, we characterize the Fano resonances directly in terms of the resonant behaviour of common pairs of PC modes.

Methods for Mitigating the Effect of Split Reference Planes on High Speed Digital System Interfaces

H. Pan[1], **H.-Y. Chao**[2], **and C. Pan**[1]

[1]Intel Corporation, USA
[2]National Chiao Tung University, Taiwan

In the past few decades, microprocessor operating frequency has increased from a few megahertz to multi gigahertz. Board-level high speed digital interfaces, such as system bus, system memory, and system I/O, that carry information between microprocessor, memory controller, I/O controller, and other components, however, have been operating at a lower frequency. This is in part because transmission line and other higher order electromagnetic effects can dominate board-level interconnect designs due to electrically significant interconnect sizes. Yet, due to the ever increasing demand for more bandwidth, operating frequencies of these board-level high speed interfaces have also been doubling in roughly two-year cycles. Parallel high speed interfaces such as Front-Side Bus (FSB) and Double Data Rate-III (DDR-3) SDRAM, for example, are fast approaching 1 GT/s, where significant frequency content can extend well into multi-GHz. In the mean time, PCI Express-like serial differential high speed interfaces, already operating at speeds over 1 GT/s, are designed into new cross-chip interconnects such as the Direct Media Interface (DMI). Routing a system with such a large number of high speed digital buses while insuring signal integrity, EMI compatibility, and ESD susceptibility, is a challenge.

While on-board interconnects are operating at much higher frequencies, the cost of the overall computing system has been decreasing. Computer manufacturers are therefore continuously looking for ways to lower the production cost. In a mobile computing system, where size is a main constraint and expensive high layer count printed circuit board (PCB) technology has been used to control routing congestion, using cheaper technologies with a smaller number of routing layers is an attractive mean of controlling manufacturing cost. On the other hand, routing on a severely size-constrained mobile platform with a smaller number of routing layers can inadvertently expose wide high speed digital interfaces to non-ideal conditions such as reference plane gaps produced by various power islands. Multi-GHz operation of these high speed signals also means that the traditional mitigation method of adding bypass capacitors across the reference gaps is becoming ineffective. In this paper, we will explore a number of other methods that can be used in conjunction with bypass capacitors to mitigate the effect of these reference plane gaps on signal quality, as well as system EMI and ESD.

Multipath Reduction of GPS Measures through Heuristic Techniques of Compensation

V. Barrile, M. Cacciola, and F. Cotroneo
University "Mediterranea" of Reggio Calabria, Italy

Abstract—The Global Positioning System, also known with the acronym GPS, is today widely used in civil and military applications, as for correct object positioning, as in other fields (ionospheric inferences, soil mapping and characterization, and so on). A limitation in the accuracy retrievable by differential GPS measures is due to multipath error which arises when GPS signal is reflected by surfaces around the antenna. In particular, many GPS receivers are projected with firmware implemented by means of classical mathematic algorithms, which can minimize multipath errors. This paper describes project criteria and experimental results obtained by a multipath rejection system based on Radial Basis Function Neural Networks, compared with measures retrieved by a commercial Differential GPS receiver.

1. Introduction

One of the most relevant source of error in GPS differential measures is due to reflection of signal coming from satellite by surfaces around GPS antenna. This phenomenon introduces a distortion in error phase measurements, which in scientific literature is normally defined as multipath error [1]. In order to reduce its influence, many solutions have been studied, working at level of elaboration of received GPS signal at ground. In order to deject multipath effect, further methods are to position GPS antennas where reflections of signal coming from GPS constellation are minimized, or to give extended ground plane to GPS antennas. In many cases, however, these solutions are practically difficult to apply: an example is the installation of a GPS antenna on a satellite in order to calculate its correct position in real-time. Nowadays, the most part of commercialized Differential GPS (DGPS) receivers are able to grant performances of multipath rejection in the order of 75%, with obtaining times averagely near of 10 s. In scientific environment there is the requirement to obtain an expert and quick inferential model, that can guarantee multipath rejection quality at least comparable to classical models, but with better flexibility and robustness qualities, smaller computational complexity and lower calculus times during regression phase, for real-time applications. Therefore, a Radial Basis Function Neural Network (RBFNN) is used to calculate multipath biases, comparing retrieved simulation results with measurements obtained by a commercial DGPS receiver. Two quantities have been considered to evaluate our RBFNN model: gaps between RBFNN simulations and DGPS measurements, and elapsed times for retrieving RBFNN results and DGPS measurements. In detail, the paper is structured according to the following schema: section 2 describes the fundamental of DGPS, with a brief explanation of multipath effect; in section 3 RBFNN are drawn up; the case study and the campaigns of measurements are respectively pointed out in section 4 and 5; section 6 is used to show RBFNN simulation results and, finally, some conclusions are illustrated in section 7.

2. Differential GPS: the Multipath Minimization Problem

The NavSTAR GPS (Navigation Satellite Timing And Ranging Global Positioning System) system was originally borne in USA for military purposes; it allows the three-dimensional positioning of objects (also moving) to be identified by means of information coming from a geostationary satellite system by using distance measuring spatial intersections (ground receiver - orbit satellite). Mainly two kinds of GPS measures can be used [2]: the pseudo-range and phase measures. GPS satellites transmit on two frequencies, L1 (1575.42 MHz) and L2 (1227.6 MHz), of which the C/A code is modulated only on L1 while the P code is modulated on both frequencies [3]. Mathematically, the pseudorange observable is formulated as follows [4]:

$$p = \rho + d\rho + c(dt - dT) + d_{ion} + d_{trop} + \varepsilon_p \tag{1}$$

where p is the measured pseudorange ([m]), ρ is the geometric range ([m]), dρ is the orbital error ([m]), c is the speed of light in ([m/s]), dt is the satellite clock error ([s]), dT is the receiver clock error ([s]), d_{ion} is the ionospheric error ([m]), d_{trop} is the tropospheric error ([m]), ε_p is the receiver code noise plus multipath ([m]). In the above equation, there are four unknowns, the three components of the user position and the receiver clock error. Thus, assuming that all other errors are either removed by modelling or are zero mean, at least four pseudoranges must be observed in order to obtain a solution. The carrier phase observable is very similar to the pseudorange observable:

$$\Phi = \rho + d\rho + c(dt - dT) + \lambda N - d_{ion} + d_{trop} + \varepsilon_\Phi \tag{2}$$

where Φ is the observed integrated carrier phase ([m]), λ is the wavelength ([m]), N is the integer ambiguity (integer number of wavelengths between the satellite and the receiver), ε_Φ is the receiver carrier phase noise plus multipath ([m]). In an attempt to reduce the errors in positioning results using equations (1) and (2), the difference between observations from two different receivers but the same satellite are considered. Therefore, the satellite clock error, is completely eliminated while the atmospheric and orbital errors are significantly reduced. This method is commonly referred to as DGPS. By further differencing the observables between satellites (see Fig. 1), the receiver clock error term is also eliminated and the double difference equations (represented by $\Delta\nabla$) become:

$$\Delta\nabla p = \Delta\nabla\rho + \Delta\nabla d\rho + \Delta\nabla d_{ion} + \Delta\nabla d_{trop} + \Delta\nabla\varepsilon_p \tag{3}$$

$$\Delta\nabla\Phi = \Delta\nabla\rho + \Delta\nabla d\rho + \lambda\Delta\nabla N - \Delta\nabla d_{ion} + \Delta\nabla d_{trop} + \Delta\nabla\varepsilon_\Phi \tag{4}$$

The main advantage of the double difference observation is that the receiver clock errors are eliminated, and ionospheric, tropospheric, and orbital errors are reduced.

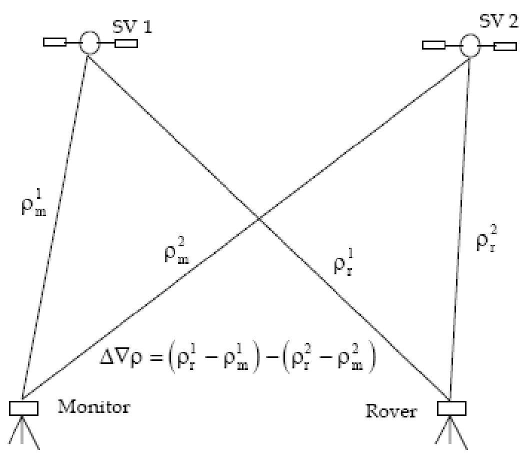

Figure 1: Graphic schematization for double differences calculation

2.1. Multipath errors

Multipath is defined as "the phenomena whereby a signal arrives at a receiver via multiple paths" [5]. It can be caused by almost any reflective surface near the antenna (Fig. 2). For short baselines (i. e. <10 km), multipath is usually the largest error source. Under severe multipath conditions, errors can reach 1 wavelength (i. e. 1 chip length) for code observations or 1/4 of a wavelength for phase observations. Recently, improvement has been made in receiver design to reduce the effect of multipath in code measurements, with percentages equal to 75% depending on the multipath delay.

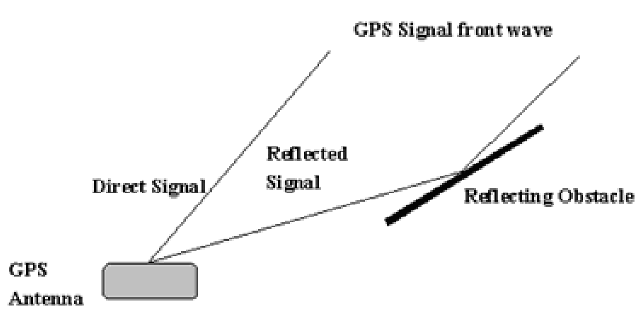

Figure 2: Graphical description of multipath phenomenon

3. Radial Basis Function Neural Networks

Adaptive Neural Networks are very good tools for non-linear approximation [6]. Neural networks are composed of simple elements operating in parallel. These elements are inspired by biological nervous systems. As in nature, the network function is determined largely by the connections between elements. Commonly neural networks are adjusted, or trained, so that a particular input leads to a specific target output. It is possible to train a neural network to perform a particular function by adjusting the values of the connections (weights) between elements. Typically many such input/target pairs are used, in this supervised learning, to train a network. Therefore, Adaptive Neural Networks are basically adaptive systems that "learn" to correctly execute a defined job (complex, non linear and multi-variable relations) by using some examples [7]. RBFNNs have capabilities to solve function approximation problems [8]. RBFNNs consist of three layers of nodes: more than input and output layers, RBFNNs have a hidden layer, where Radial Basis Functions are applied on the input data. A schematic representation of RBFNN is described in Fig. 3:

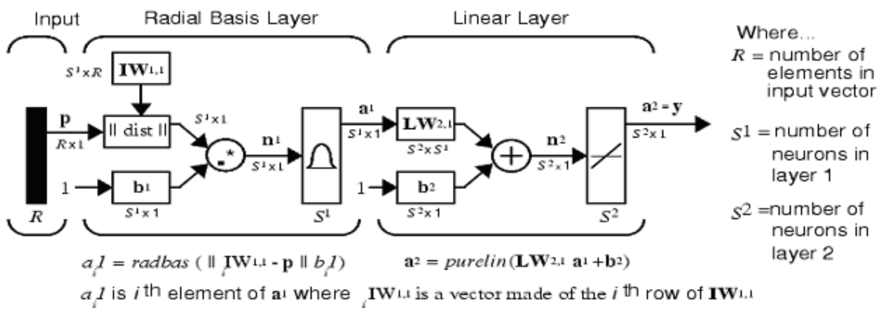

Figure 3: RBFNN schema

The $\|dist\|$ box in this figure accepts the input vector p and the input weight matrix $\mathrm{IW}^{1,1}$, and produces a vector having S^1 elements. The elements are the distances between the input vector and vectors ${}_i\mathrm{IW}^{1,1}$ formed from the rows of the input weight matrix. We can understand how this network behaves by following an input vector p through the network to the output a^2. If we present an input vector to such a network, each neuron in the radial basis layer will output a value according to how close the input vector is to each neuron's weight vector. Thus, radial basis neurons with weight vectors quite different from the input vector p have outputs near zero. These small outputs have only a negligible effect on the linear output neurons. In contrast, a radial basis neuron with a weight vector close to the input vector p produces a value near 1. If a neuron has an output of 1 its output weights in the second layer pass their values to the linear neurons in the second layer. In fact, if only one radial basis neuron had an output of 1, and all others had outputs of 0's (or very close to 0), the output of the linear layer would be the active neuron's output weights. This would, however, be an extreme case. Typically several neurons are always firing, to varying degrees.

4. The Case Study

Faculty of Engineering of University "Mediterranea" of Reggio Calabria (Italy) activated a stable network to monitor relative movements of Sicilian and Calabrian shores inner the area of Stretto di Messina by means GPS techniques. Since vertexes of a main network cannot make movements in the order of the measure uncertainty ($10^{-6} \div 10^{-7}$), it has been necessary to implement a control subnet for each main vertex. One of these subnets is composed by 4 vertexes (Fig. 4); they are located in a surely stable area with an optimal visibility of satellites. It has been chosen short bases in order to avoid tropospheric and ionospheric errors; but it has been retrieved multipath errors in base 2-4, due to reflecting surfaces near one of the vertexes.

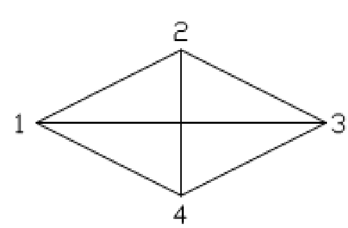

Figure 4: Control subnet implemented to guarantee stability of main network

Therefore, it has been exploited a RBFNN-based system in order to minimize multipath errors, evaluating multipath as a function of other GPS quantities. RBFNNs are able to approximate the trend of a function after a training procedure, which is carried out by a collection of data examples. Therefore, it is necessary to make a measurement campaign in order to implement a dataset of training (DBTrain) and another to test the behavior of RBFNN (DBTest).

5. Data Collection Campaign and RBF Simulation Results

The data collection campaign has been carried out inner the area described on section 4, by means of a L1/L2 GPS antenna without multipath rejection, in two different days (acquisition times about equal to 24 hours). Multipath error has subsequently been calculated by means of equation (5), representing a simplified schematization of phase differential measure:

$$b \bullet s = m\lambda + \Delta\varphi + \Delta\varphi_{ric} + \Delta\varphi_{bias} + \Delta\varphi_{mp} \tag{5}$$

where b is baseline direction; s is the arrival direction of GPS signal; $\Delta\varphi$ is the fractional part of phase differential measure (observable); $\Delta\varphi_{ric}$ is the receiver noise (white noise with standard deviation approximately equal to 1-2 mm.); $\Delta\varphi_{bias}$ is the bias noise, considered as a constant (autocalibration procedure); $\Delta\varphi_{mp}$ is the multipath error (highly correlated coloured noise). It is possible to obtain the $\Delta\varphi_{mp}$ value expressed in degree for each base, by a comparison with the opportune "nominal reference" and after approximations of bias and noise in equation (5). Moreover, it is necessary to verify that approximations influence the measure value without changing it, if the measure is compared by means of different antennas. This value is calculated by exploiting the position of the two receivers and the satellite providing GPS signal; the satellite position is defined by azimuth and elevation and is retrievable by ephemeredes of GPS signal. By using a classical GPS antenna without multipath rejection, a set of measurements has been carried out in different places of Reggio Calabria, Italy. So, a set of values has been collected for each of the following quantities (see eq. 5): b, $\Delta\varphi$, $\Delta\varphi_{ric}$, $\Delta\varphi_{bias}$; let us define, for each measurement, these quantities as an input pattern. Subsequently, by using equations (5), (4) and (2) the $\Delta\varphi_{mp}$ values (output patterns) has been calculated, and each input pattern has been linked to its proper output pattern, making a so called data pattern. So, a set of 1500 data patterns has been collected in order to implement the database used for training phase of RBFNN. The trained RBFNN retrieved by Neural Network Matlab Toolbox has been subsequently tested inner the base 2-4 (Fig. 4). Specifically, it has been considered mean, standard deviation and Round Mean Square (RMS) of errors introduced by $\Delta\varphi_{mp}$. They have been obtained after the elaboration of raw data during the 24 hours of acquisition using all visible satellites. Retrieved results demonstrate a reduction of multipath effect in average equal to 45%, in standard deviation of 20% and in RMS of 25%. Moreover, performances of our approach have been tested measuring the slope distance of base 2-4. Measure retrieved by RBFNN-based system has been compared with ones retrieved by a LEICA SR530 receiver.

Table 1 shows the measurements retrieved by LEICA SR530 and our RBFNN-based system for multipath rejection, compared with actual slope distance measured by classical techniques. Performances of our RBFNN-based system are also evaluated by a comparison of elapsed times to obtain 2-4 slope distance with the used commercial GPS receiver (Table 2).

Table 1: Slope distance of base 2-4

	Actual	LEICA SR530	RBFNN-based System
Slope distance 2-4 (meters)	50.000 ± 0.0001	50.12 ± 0.0001	50.004 ± 0.0001

Table 2: Elapsed times to obtain 2-4 slope distance

LEICA SR530	RBFNN-based System
10 seconds	1.2 second

6. Conclusions and Future Works

In this article, the problem of multipath in GPS measures has been analyzed. This is a very significant problem, above all when application field needs a great accuracy in GPS observation. By means of a classical GPS antenna, measurement campaigns has been carried out, and an heuristic system based on RBFNN has been considered in order to reject multipath effects. Performances of our RBFNN-based system for multipath rejection has been evaluated during the acquisition period and compared with measurements retrieved by commercial receiver LEICA SR530. Retrieved results show the following advantages of RBF approach:

- during the 24 hours of acquisition, the RBFNN-based system allows a reduction of multipath effect averagely equal to 30%;
- concerning the calculation of slope distance for base 2-4, a reduction of measure error about equal to 0.234% is obtained exploiting our RBFNN approach against the LEICA receiver;
- RBFNN-based system shows lower elaboration times than LEICA receiver; it is due to the lower computational complexity of the RBFNN-based system

Therefore, the usage of RBFNNs to reduce multipath errors show very interesting results, even if, considering the approximations in (5) for bias and noise, they would have to be verified according to the application environment. Moreover, a further development will be the hardware deployment on FPGA of trained RBFNN, in order to build a Special Purpose Chip (SPC). The aim is to integrate the SPC into a GPS receiver without multipath minimization capabilities, in order to compare its performances with ones obtained by a multipath rejection antenna.

REFERENCES

1. Tranquilla, J. M., "Multipath and imaging problems in GPS receivers antennas," *IV Int. Geodetic Symposium on Satellite Positioning*, Vol. 1, 557–571, 1986.
2. Hoffman-Wellenhof, et al., *GPS Theory and Practice*, Springer-Verlag, New York, 1997.
3. Parkinson, B. W., *Introduction and Heritage of NAVSTAR, the Global Positioning System, Global Positioning System: Theory and Applications*, Vol. 1, Ch. 1, American Institute of Aeronautics and Astronautics, Inc., Washington, 1996.
4. Wells, D. E., et al., *Guide to GPS Positioning, 2nd printing with corrections*, Canadian GPS Associates, Fredericton N. B., 1987.
5. Qiu, W., *An Analysis of Some Critical Error Sources in Static GPS Surveying*, UCGE Reports No. 20054, Department of Geomatics Engineering, University of Calgary, 1993.
6. Bishop, C., *Pattern Recognition and Neural Networks*, Oxford University Press, 1995.
7. Murray, R., D. Neumerkel, and D. Sbarbaro, "Neural networks for modeling and control of a non-linear dynamic system," *Proceedings of the 1992 IEEE International Symposium on Intelligent Control*, 404–409, 1992.
8. Chen, S., C. F. N. Cowan, and P. M. Grant, "Orthogonal least squares learning algorithm for radial basis function networks," *IEEE Transactions on Neural Networks*, Vol. 2, No. 2, 302–309, 1991.

Accurate Analysis of Practical Diffraction Gratings

H. A. Kalhor and M. R. Zunoubi
State University of New York, USA

Diffraction gratings have been used in many applications including spectroscopy for many years. Many ingenious approximate, analytical, and numerical techniques have been devised and used for their analysis. However, most of the proposed techniques used idealized models. The structures have been considered infinitely periodic, perfectly conducting and without groove shape imperfections. Attempts have been made to incorporate some imperfections such as finite conductivity and groove shape errors in the idealized models with some success [1–4]. Theoretical and measurement results, however, did not agree in many cases and certain anomalous behavior could not be explained. More recently, a method based on impedance boundary conditions has been proposed to analyze finite planar and curved frequency selective surfaces [5].

Recent developments of new and powerful numerical methods have empowered researchers to study the effects of these imperfections more accurately, and revisiting these classical problems seems in order.

The object of this presentation is to study the performance of practical gratings with all their associated imperfections accurately. A few numerical techniques will be employed and compared and contrasted. The behavior of reflection diffraction gratings of practical interest such as echelette sinusoidal, and lamellar as well as transmission gratings made of wire grids, conducting cylinders, and conducting bars will be studied. Comparison with experimental results will be made where possible.

REFERENCES

1. Kalhor, H. A. and A. R. Neureuther, "Effects of conductivity, groove shape, and physical phenomena on the design of diffraction grating," *J. Opt. Soc. Am.*, Vol. 63, No. 11, 1412–1418, 1973.
2. Christodoulou, C. and J. Kauffman, "On the electromagnetic scattering from infinite rectangular grids with finite conductivity," *IEEE Trans. Antennas Propag.*, Vol. 34, No. 2, 144–154, Feb. 1986.
3. Abboud, T. and H. Ammari, "Diffraction at a curved grating: approximation by an infinite plane grating," *J. Math. Anal. and App.*, Vol. 202, 1076–1100, 1996.
4. Whites, K. W. and R. Mittra, "An equivalent boundary-condition model for lossy planar periodic structures at low frequency," *IEEE Trans. Antennas Propag.*, Vol. 44, No. 12, 1617–1629, Dec. 1996.
5. Stupfel, B. and Y. Pion, "Impedance boundary conditions for finite planar and curved frequency selective surfaces," *IEEE Trans. Antennas Propag.*, Vol. 53, No. 4, 1415–1425, April 2005.

Spectrum Properties of Partially Coherent Modified Bessel-Gauss Beams by a Lens with Aperture

X. R. Lin
Fuzhou University, China

Q. S. Wang
FuJian Dragon Enterprises Co., Ltd, China

C. Y. Peng
Putian University, China

Starting from the propagation equation of partially coherent light, the spectral shift and spectral switch of partially coherent modified Bessel-Gauss beams passing through a lens with aperture are studied. Numerical results show that the on-axis spectrum in the near zone is different from the spectrum of the source, and the on-axis spectrum in the near zone is split into multi-peaks. It is also found that the spectral shift shows a gradual change. However, when z_f approaches a critical value, a rapid spectral transition occurs. The effect is called spectral switch. For example, when the parameters for calculation are the central frequency of the spectrum $\omega_0 = 3.2 * 10^{15} s^{-1}$, effective coherence length on the source plane $\sigma_0 = 0.6 * 10^{15} s^{-1}$, Fresnel number of beam $N_w = 1$, the spectral degree of coherence $\xi = 0.5$, and truncation parameter $\delta = 0.3$. For the axial spectrum at $z_f = 0.0105$, the relative spectral shift is bigger than zero, and the blue shift occurs. The two major peaks reach the same height at the critical point $z_f = 0.0111$, and the subordinate peaks separately at the both sides of major peaks also reach the same height. This means that the spectral shift is transformed from the blue shift to the red shift, and the spectral switch occurs at this point. With the increase of z_f, the red shift decreases. When z_f equals 0.0127, the spectral shift equals 0. When z_f equals 0.0148, the spectral switch occurs again. The distance between the major peaks when z_f equals 0.0127 is larger than that when z_f equals 0.0111. Numerical results also show that the spectral switch positions and the spectral switch performance of partially coherent modified Bessel-Gauss beams depend on the spectral degree of coherence, Fresnel number of beam and truncation parameter. The number of spectral switch increases with the increase of the Fresnel number of beam, and decreases with the increase of the spectral degree of coherence.

Generalized Lorenz-Mie Theory for the Arbitrarily Oriented Shaped Beam Scattering by a Spheroid

F. Xu[1,2], **K. F. Ren**[2], **and X. S. Cai**[1]

[1]University of Shanghai for Science and Technology, China
[2]Université et INSA de Rouen, France

Light scattering by a spheroid was firstly studied by S. Asano, et al., [1]. It was extended to the case of arbitrary shaped beam scattering by J.P. Barton [2], who described the incident field through "surface integrals". Within the framework of generalized Lorenz-Mie theory (GLMT) [3], on-axis and off-axis Gaussian beam scattering by a spheroid was also studied by Han, et al., [4, 5].

In the present paper, the scattering of a shaped beam with arbitrary orientation relative to a spheroidal particle is developed within the framework of GLMT, i. e., the arbitrarily oriented incident beam is firstly expressed by the beam shape coefficients (BSC) in spherical coordinates. Then the BSC is transformed to the spheroidal coordinates, thanks to the relationship between the spherical wave vectors ($\mathbf{m}_{mn}$, $\mathbf{n}_{mn}$) [6] and the spheroidal ones ($\mathbf{M}_{mn}$, $\mathbf{N}_{mn}$) [7].

But we found that for BSC evaluation by the localization approximation is no longer valid for the oblique incidence. So the quadrature method is applied instead. Besides, for the sake of consistence with Lorenz-Mie theory, time dependence of $\exp(i\omega t)$ is used, instead of $\exp(-i\omega t)$ in GLMT. The relationship of the BSC in two different time conventions are carefully examined and a simple relationship is found.

Finally, numerical results of the scattered intensity in far field are presented. They are found coincident with those in the cases of both oblique plane wave incidence on a spheroid [1] and shaped beam incidence on a sphere [3].

REFERENCES

1. Asano, S. and G. Yamamoto, "Light scattering by a spheroidal particle," *Appl. Opt.*, Vol. 14, 29–49, 1975.
2. Barton, J. P., "Internal and near-surface electromagnetic fields for a spheroidal particle with arbitrary illumination," *Appl. Opt.*, Vol. 34, 5542–5551, 1995.
3. Gouesbet, G., B. Maheu, and G. Gréhan, "Light scattering from a sphere arbitrarily located in a Gaussian beam, using a Bromwich formulation," *J. Opt. Soc. Am. A*, Vol. 5, 1427–1443, 1988.
4. Han, Y. P. and Z. Wu, "Scattering of a spheroidal particle illuminated by a Gaussian beam," *Appl. Opt.*, Vol. 40, 2501–2509, 2001.
5. Han, Y. P., G. Gréhan, and G. Gouesbet, "Generalized Lorenz-Mie theory for a spheroidal particle with off-axis Gaussian-beam illumination," *Appl. Opt.*, Vol. 42, 6621–6629, 2003.
6. Stratton, J. A., *Electromagnetic Theory*, McGraw-Hill, NewYork, 1941.
7. Flammer, C. and U. Press, *Spheroidal Wave Functions*, Stanford, Calif., 1957.

The Radiated Emission Approach to Specific Emitter Identification

J. Dudczyk and M. Wnuk
Military University of Technology, Poland

The modern ESM/ELINT systems should be able to recognise emitters on the basis of the set of pulse measurements in order to provide surveillance, tracking and platform identification. One of the most principal functions of the ESM system is gathering basic information from entire electromagnetic spectrum and analysing communication and non-communication emitter's characteristics such as their technical parameters, operating role and main tasks. In this analysis there are of special importance methods of data acquisition. The methods of Specific Emiter Identification (SEI) are based on the Measurement and Signature Intelligence (MASINT). Non-intentional emission (calls–radiated emisssion) is a source of knowledge about the analysed emitter. Such information is crucial during the process of emitter identification. The results of classification and identification are presented on a display in a form of tabular or grapfical options.

This paper provides an overview of the methods of radiated emission measurement, for example: Open Area Test Site (OATS), full and semi anechoic chambers, Transverse Electromagnetic Cell (M. L. Crawford Cell–TEM) and Gigahertz Transverse Electromagnetic Cell (GTEM), which may be used to identify radar's equipment.

This paper presents selected aspects of radiated emission acquisiton (in a specially prepared procedure), analysis of their parameters, features extraction using "special linear transformation". According to the presented method of transformation, the "measured function $K(f_n)$" is determined. The function $K(f_n)$ is used to extract radiated emission features, which modify structure of Extended Vector Parameters (EVP). At the end of the procedure, radar emitter source identification is performed. During the process of emitter identification distance functions (Euclidean, Mahalanobis, Hamming) are applied. The process of recognition is connected with the data base, which is an important element in the modern electronic intelligence system. Dinstinctive features extraction from radiated emission is used for special "radar signature" description in the data base.

Taking all above into consideration, applying the radiated emission to the specific emitter identification is an essential element in formation of the examined system. The capability of an ESM/ELINT system to correctly identify detectable radar emissions in a dense environment is key to their application in modern commmand, communication and control system. The problem of radiated emission is essential with respect to Electro-Magnetic Compatibility (EMC).

Backscattering from Rectangular Plates Illuminated at Grazing Incidence

R. A. Ross
17A Phillips Drive, Westford, MA, 01886, USA

A formula is presented for predicting monostatic scattering from rectangular plates at grazing incidence with vertical polarization. The formula uses the Geometrical Theory of Diffraction to describe returns from the front and rear of the plate. The contribution from the rear edge is associated with a new form of double diffraction. Predictions are compared with numerical results from the Method of Moments for objects between 2 and 18 wavelengths in extent. When predicting the characteristic oscillation in RCS of rectangular plates as a function of width, accuracy increases with increase in the height of the plate. When plates are both short and wide, theory underestimates the RCS of peaks.

Optimized Satellite System-like Data Fitting on a Spherical Shell

J. Sanchez-Mondragon[1], **B. Wolf**[2], **M. Tecpoyotl-Torres**[3]
J. Escobedo-Alatorre[3], **and M. Torres-Cisneros**[4]
[1]Instituto Nacional de Astrofísica, Óptica y Electrónica (INAOE), Mexico
[2]UNAM, Mexico
[3]Universidad Autónoma del Estado de Morelos, Mexico
[4]FIMEEE, México

Abstract—The measurement of irradiance on a spherical shell is a common in different fields that goes from geological, biological and many others. Accuracy depends of a judicious use of the sampling, and the last is often defined by technical limitations due to the available infrastructure in each field. Such is the case of the so called planetary array, described as a set of satellite like trajectories on the spherical shell. Both, the data acquisition and the ideal data base, in this case spherical harmonics, may be optimized. The measured points are distributed over maximal circles obtained from the equator, and each other are related by the corresponding rotations. Each circle has 2L+1 equidistant points (the first one and the last one coincides), and the field on the sphere is adjusted by the determination of the harmonic coefficients, as an optimization problem, with Nc equation systems of 2L+1 simultaneous equations for $(L+1)^2$ variables.

1. Introduction

We had previously analyzed the problem of the irradiance measurement under circular and spherical geometries, considering a uniform sensor detection system [1]. Now, we are trying to measure a field F, on the surface of the Earth using a spherical detection system. The detectors are localized on trajectories, which are obtained by rotations over the equator, as it is shown in Fig. 1, but the arrangement of the detectors is not uniform distributed on the trajectories as in our earlier spherical experiments.

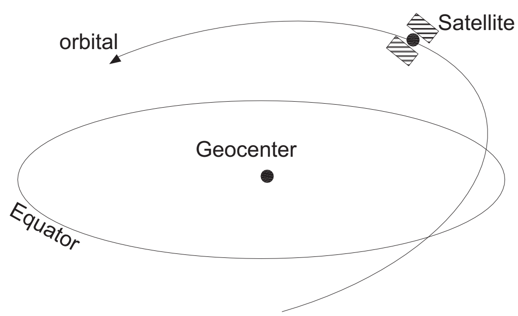

Figure 1: One of the detectors of the proposed spherical detection system.

The analysis of the new system requires the mathematics development that is described as follows:

At first, we consider an observable $F(\theta_n;\phi_n)$ over a determined number of points in the sphere. The points of measurement are distributed over N_c maximal circles, which are obtained since rotations from the equator C^0 (defined by $\theta = \frac{1}{2}\pi$ and $0 \le \phi < 2\pi$):

$$C^{(\alpha_j,\beta_j,\gamma_j)} := R(\alpha_j,\beta_j,\gamma_j) : C^0 \tag{1}$$

by Euler angles $(\alpha_j,\beta_j,\gamma_j)$, $j = 1, 2, ..., N_c$. The normal lines to these circles are (β_j,γ_j) on the sphere, and its phases are α_j respect to the Greenwich meridian.

Over each circle there are distributed an odd number $2L+1$ of equidistant points, where we measured the value of $F(\theta_n;\phi_n)$. In this way, we can calculate its $2L+1$ Fourier coefficients G_m through the FFT [2]. For the equator case C^0, we calculate:

$$\widetilde{F}^0_m := \frac{1}{\sqrt{2l+1}}\sum_{n=-L}^{L} F(\frac{1}{2}\pi,\phi_n)e^{i(m\phi_n)}, \quad \text{where} \quad \phi_n := \frac{2\pi n}{2L+1}, \tag{2}$$

with $n, m \in \{-L, -L+1, ..., L\}$ module $2L+1$ in the symmetrical interval f cycling. The Fourier synthesis is given by:

$$F(\frac{1}{2}\pi, \phi_n) = \frac{1}{\sqrt{2L+1}} \sum_{m=-L}^{L} \widetilde{F}_m^0 e^{-im\phi_n}. \tag{3}$$

On the maximal circles $C^{(\alpha_j,\beta_j,\gamma_j)}$ we will have the measurements and calculations of the $2L+1$ corresponding coefficients, $\widetilde{F}_m^{(\alpha_j,\beta_j,\gamma_j)}$, $m\,|_{-L}^{L}$, $j\,|_{1}^{N_c}$.

The F field over the sphere under measurement has a development in spherical harmonics truncated at L value, given by:

$$F(\theta, \phi) = \sum_{\ell=0}^{L} \sum_{m=-\ell}^{\ell} F_{\ell,m} Y_{\ell,m}\ . \tag{4}$$

The number of elements in the series is $1+3+5+\cdots+(2L+1) = (L+1)^2$. The question is: How we can calculate the $(L+1)^2$ coefficients of spherical harmonics $F_{\ell,m}$ in terms of the $N_c(2L+1)$ coefficients $\widetilde{F}_m^{(\alpha_j,\beta_j,\gamma_j)}$ obtained over the circles?

In the following section we present the development over the equator, in section 3 we present the rotation over any maximal circle, and in section 4 we compare the obtained results.

2. Development over the Equator

The spherical harmonics are given by:

$$Y_{\ell,m}(\theta, \phi) = (-1)^m \sqrt{(\ell+2)(\ell+m)!(\ell-m)!}\, \frac{e^{im\phi}}{\sqrt{2\pi}} \times \sum_k \frac{(-1)^k (\sin\theta)^{2k+m}}{2^{k+m}(k+m)!k!} \frac{(\cos\theta)^{\ell-2k-m}}{(\ell-2k-m)!}\ . \tag{5}$$

The factorials implies that the addition is over all integers k among $max(-m, 0)$ and $\frac{1}{2}(\ell-|m|)$, the number of elements in the addition is given by $\frac{1}{2}(\ell-|m|)+1$ (where $|x|$ is the integer part of x). Over the equator $\theta = \frac{1}{2}\pi$, the factor $(\cos\theta)^{\ell-2k-m}$ is different of zero, only when its power is zero, *id est* $k = \frac{1}{2}(\ell-m)$ with $\ell-m$ even. Then:

$$Y_{\ell,m}(\frac{1}{2}\pi, \phi) = y_{\ell,m} \frac{e^{im\phi}}{\sqrt{2\pi}}, \quad y_{\ell,m} = y_{\ell,-m}, \tag{6}$$

$$Y_{\ell,m} := \begin{cases} (-1)^{(\ell+m)/2} \frac{\sqrt{(\ell+\frac{1}{2})(\ell+m)!(\ell-m)!}}{2^\ell(\frac{1}{2}[\ell+m])!((\frac{1}{2}[\ell-m])!)} & \ell \pm m \text{ even} \\ 0, & \ell \pm m \text{ odd}\ . \end{cases} \tag{7}$$

Over the equator C^0, the field $F(\theta, \phi)$ development in a different of zero harmonics series (4) is:

$$\begin{aligned} F(\frac{1}{2}\pi, \phi) &= \sum_{\ell=0}^{L} \sum_{m=-\ell}^{L} F_{\ell,m} Y_{\ell,m}(\frac{1}{2}\pi, \phi), && \Big(\text{the harmonics of zero value in } C^0 \text{ are absent} \\ &= \sum_{m=-\ell}^{L} \frac{e^{im\phi}}{\sqrt{2\pi}} \sum_{\substack{\ell=|m| \\ \ell-m \text{ even}}}^{L} F_{\ell,m}\, y_{\ell,m}, && \Big(\text{interchanging additions } \ell \text{ and } m \\ &= \frac{1}{\sqrt{2L+1}} \sum_{m=-\ell}^{L} e^{im\phi} \widetilde{F}_m^0\ , && \Big(\text{in agreement with (3) considering } \phi_n = 2\pi n/(2L+1). \end{aligned} \tag{8}$$

Comparing the last two terms, related with the coefficients introducing the $2L+1$ measured/calculated data:

$$G_m^0 := \sqrt{\frac{2\pi}{2L+1}}\, \widetilde{F}_m^0 = \sum_{\substack{\ell=|m| \\ \ell-m \text{ even}}}^{L} F_{\ell,m}\, y_{\ell,m}, \quad m\,|_{-L}^{L}. \tag{9}$$

Here we have the key relationships among the $2L+1$ coefficients $\{G_m^0\}_{m=-L}^{L}$ measured/calculated over the equator, and the $(L+1)^2$ coefficients $\left\{F_{\ell,m}\right\}_{m=-\ell,\ell=0}^{\ell \quad L}$ of the spherical harmonic development that we are looking for. The harmonics with $\ell - m$ even are absent, which have one of their nodal circles over the equator.

As an example we consider the case with $L = 3$ Then we have the development with 16 spherical harmonics:

$$Y_{0,0},\ \{Y_{1,m}\}_{m=-1}^{1},\ \ \{Y_{1,m}\}_{m=-2}^{2},\ \text{and}\ \{Y_{1,m}\}_{m=-3}^{3}$$

with their corresponding coefficients $F_{\ell,m}$.

On the other side, we have the 7 measured/calculated coefficients $\left\{G_m^0\right\}_{m=-3}^{3}$, $\left\{G_m^0\right\} = \sqrt{2\pi/7}\,\widetilde{F}_m^0$. The equations (9) are then:

$$\begin{array}{lllllll}
G_3^0 = F_{3,3}\ y_{3,3} & m=3 & & & & \bullet & \\
G_2^0 = F_{2,2}\ y_{2,2} & m=2 & & & \bullet & \circ & \\
G_1^0 = F_{1,1}\ y_{1,1} + F_{3,1}\ y_{3,1} & m=1 & & \bullet & \circ & \bullet & \\
G_0^0 = F_{0,0}\ y_{0,0} + F_{2,0}\ y_{2,0} & m=0 & \bullet & \circ & \bullet & \circ & \longrightarrow \ell \\
G_{-1}^0 = F_{1,-1}\ y_{1,-1} + F_{3,-1}\ y_{3,-1} & m=-1 & & \bullet & \circ & \bullet & \\
G_{-2}^0 = F_{2,-2}\ y_{2,-2} & m=-2 & & & \bullet & \circ & \\
G_{-3}^0 = F_{3,-3}\ y_{3,-3} & m=-3 & & & & \bullet &
\end{array} \tag{10}$$

The right diagram shows the structure of the present terms $\bullet$ in the truncated series, and the absent ones $\circ$.

The equations used to calculate the 16 [that is, the $(L+1)^2$] coefficients of the harmonic series $F_{\ell,m}$ are divided in three groups: are divided in three groups:

- **Determined**: $F_{3,\pm 3}$ and $F_{2,\pm 2}$ Always are 4: $F_{L,\pm L}$ and $F_{L-1,\pm(L-1)}$.
- **In linear combination**: $F_{1,1} \leftrightarrow F_{3,1}$, $F_{0,0} \leftrightarrow F_{2,0}$, $F_{1,-1} \leftrightarrow F_{3,-1}$. Generally For $|m| \leq L-2$, there are $F_{\ell,m} \leftrightarrow F_{\ell',m}$ with $0 \leq \ell \leq \ell' \leq L$. In the horizontal line m of the diagram (10), there are a total of $\frac{1}{2}[(L-|m|)]+1$ coefficients in linear combination. There are a total of $\frac{1}{2}(L^2+3L-6)$ $F_{\ell,m}$ coefficients that we known only inside of linear combinations.
- **Undetermined**: $F_{3,\pm 2}$, $F_{2,\pm 1}$, $F_{1,0}$, and $F_{3,0}$. Generically, they are the known $F_{\ell,m}$ with $\ell - m$ odd, whose spherical harmonics are zero in the equator, and the number of them is $\frac{1}{2}L(L+1)$.

3. Development over the Circle $C^{(\alpha,\beta,\gamma)}$

In this section, we rotate this maximal circle as it is presented in equation (1) in order to obtain the generic circle $C^{(\alpha,\beta,\gamma)}$.

Under the rotation by means of the Euler angles (α, β, γ), the spherical harmonics showed in equation (4) of each ℓ order, is transformed as:

$$Y_{\ell,m}(\theta',\phi') = [R(\alpha,\beta,\gamma) : Y_{\ell,m}](\theta,\phi) = \sum_{m'=-\ell}^{\ell} D_{m,m'}^{\ell}(\alpha,\beta,\gamma) : Y_{\ell,m'}(\theta,\phi), \tag{11}$$

where the rotation of the polar coordinates in the sphere is:

$$\begin{pmatrix} \sin\theta'\cos\phi' \\ \sin\theta'\sin\phi' \\ \cos\theta' \end{pmatrix} = \begin{pmatrix} \cos\alpha & -\sin\alpha & 0 \\ \sin\alpha & \cos\alpha & 0 \\ 0 & 0 & 1 \end{pmatrix} \begin{pmatrix} \cos\beta & 0 & \sin\beta \\ 0 & 1 & 0 \\ -\sin\beta & 0 & \cos\beta \end{pmatrix} \times \begin{pmatrix} \cos\gamma & -\sin\gamma & 0 \\ \sin\gamma & \cos\gamma & 0 \\ 0 & 0 & 1 \end{pmatrix} \begin{pmatrix} \sin\theta\cos\phi \\ \sin\theta\sin\phi \\ \cos\theta \end{pmatrix}. \tag{12}$$

And the coefficients of the linear combination are the functions D of Wigner, $D_{m,m'}^{\ell}(\alpha,\beta,\gamma)$, which is factorized as:

$$D_{m,m'}^{\ell}(\alpha,\beta,\gamma) = e^{-im\alpha} d_{m,m'}^{\ell}(\beta) e^{-im'\gamma}. \tag{13}$$

In terms of phases, for α and γ, and the little-D of Wigner, $d^{\ell}_{m,m'}(\beta)$, given by:

$$d^{\ell}_{m,m'}(\beta)=\sqrt{(\ell+m)!(\ell-m)!(\ell+m')!(\ell-m')!}\sum_{k}(-1)^{m-m'+k}\frac{(\sin\frac{1}{2}\beta)^{2k+m-m'}}{(k+m-m')!k!}\frac{(\cos\frac{1}{2}\beta)^{2\ell+m'-m-2k}}{(\ell-m-k)!(\ell+m'-k)!}. \tag{14}$$

The k index of the addition takes the integer values among the values: $\max(m'-m,0)\leq k\leq\min(\ell-|m|,\ell-|m'|)$. The little-$d$ coefficients satisfy many relationships, such as:

$$d^{\ell}_{m,m'}(\beta)=d^{\ell}_{m,m'}(-\beta)=d^{\ell}_{-m',-m}(\beta)=(-1)^{m-m'}d^{\ell}_{-m,-m'}(\beta), \tag{15}$$

and they are related with the spherical harmonics by:

$$Y_{\ell,m}(\theta,\phi)=\sqrt{\frac{2L+1}{4\pi}}d^{\ell}_{m,0}(\theta)e^{jm\phi}. \tag{16}$$

They satisfy recurrence S of three terms in m and m':

$$\sqrt{(\ell-m')(\ell+m'+1)}\sin\beta d^{\ell}_{m,m'+1}(\beta)+2(m-m'\cos\beta)d^{\ell}_{m,m'}(\beta)+\sqrt{(\ell+m')(\ell-m'+1)}\sin\beta d^{\ell}_{m,m'-1}(\beta)=0 \tag{17}$$

$$\sqrt{(\ell-m)(\ell+m+1)}\sin\beta d^{\ell}_{m+1,m'}(\beta)-2(m'-m\cos\beta)d^{\ell}_{m,m'}(\beta)+\sqrt{(\ell+m)(\ell-m+1)}\sin\beta d^{\ell}_{m-1,m'}(\beta)=0 \tag{18}$$

The harmonics $Y_{\ell,m}$ are transformed as a column vector. Under the rotation matrix $\|D^{\ell}_{m,m'}\|$, then, the coefficients $F_{\ell,m}$ of the series (4), that we are trying to find, are transformed as a row vector:

$$F'_{\ell,m}=[R(\alpha_j,\beta_j,\gamma_j):F]_{\ell,m}=\sum_{m'=-\ell}^{\ell}F_{\ell,m'}D_{m',m}(\alpha,\beta,\gamma). \tag{19}$$

The equator has been transformed in the circle $C^{(\alpha,\beta,\gamma)}$, nd over it, we make the measurements/calculations of the corresponding coefficients $G^{(\alpha,\beta,\gamma)}_{m}$, in the same way as in G^{0}_{m}, given by equation (10). So, we have, as in (9):

$$G^{(\alpha,\beta,\gamma)}_{m}=\sum_{\substack{\ell=|m|\\ \ell-m\text{ even}}}^{L}F'_{\ell,m}\,y_{\ell,m}=\sum_{\substack{\ell=|m|\\ \ell-m\text{ even}}}^{L}y_{\ell,m}\sum_{m'=-\ell}^{L}F_{\ell,m'}D^{\ell}_{m',m}(\alpha,\beta,\gamma). \tag{20}$$

The arrangement of the two additions can not be made directly, but in generic form, it can be written in terms of the column vectors:

$$F_{0,0},\ F_{1,\cdot}:=\begin{pmatrix}F_{1,1}\\F_{1,0}\\F_{1,-1}\end{pmatrix},\ F_{2,\cdot}:=\begin{pmatrix}F_{2,2}\\F_{2,1}\\F_{2,0}\\F_{2,-1}\\F_{2,-2}\end{pmatrix},\ \ldots\ F_{\ell,\cdot}:=\begin{pmatrix}F_{\ell,\ell}\\F_{\ell,\ell-1}\\F_{\ell,\ell-2}\\\vdots\\F_{\ell,-\ell}\end{pmatrix}, \tag{21}$$

and the row vectors:

$$D^{\ell}_{\cdot,m}:=(D^{\ell}_{\ell,m}\ D^{\ell}_{\ell-1,m}\ D^{\ell}_{\ell-2,m}\ \ldots\ D^{\ell}_{-\ell,m}). \tag{22}$$

The equations (20), which related to the spherical harmonic coefficients $F_{\ell,m}$ that we are trying to find, and the measured/calculated coefficients $G_m\equiv G^{(\alpha,\beta,\gamma)}_{m}$ over the maximal circle, are obtained from equation (10) changing $F_{\ell,m}$ by $F'_{\ell,m}$ in accordance with equation (19). The sub-matrix representation can be compared with the case $L=3$:

$$\begin{pmatrix}G^{(\omega)}_{3}\\G^{(\omega)}_{2}\\G^{(\omega)}_{1}\\G^{(\omega)}_{0}\\G^{(\omega)}_{-1}\\G^{(\omega)}_{-2}\\G^{(\omega)}_{-3}\end{pmatrix}=\begin{pmatrix}0&0&0&y_{3,3}D^{3}_{\bullet,3}\\0&0&y_{2,2}D^{2}_{\bullet,2}&0\\0&y_{1,1}D^{1}_{\bullet,1}&0&0\\y_{0,0}&0&y_{2,0}D^{2}_{\bullet,0}&0\\0&y_{1,-1}D^{1}_{\bullet,-1}&0&y_{3,-1}D^{3}_{\bullet,-1}\\0&0&y_{2,-2}D^{2}_{\bullet,-2}&0\\0&0&0&y_{3,-3}D^{3}_{\bullet,-3}\end{pmatrix}\begin{pmatrix}F_{0,\bullet}\\F_{1,\bullet}\\F_{2,\bullet}\\F_{4,\bullet}\end{pmatrix}. \tag{23}$$

The matrix is not square, it has 7 rows and its 4 columns represent the $1 + 3 + 5 + 7 = 16$ columns of the developed matrix, which generically is of $(2L + 1) \times (L + 1)^2$.

When we calculate the elements of the matrix (23), we use the properties $y_{\ell,m} = y_{\ell,-m}$ and the recurrence property mentioned in equation (15).

4. Equation Systems

Over the equator and in respect to the Greenwich meridian, the equation system (23) obtains again it most simple representation, as in equation (10), since $D^{\ell}_{m,m'}(0, 0, 0) = \delta_{m,m'}$ After each rotation, however, the number of determined, in linear combination and the undetermined coefficients are the same (for $L = 3, 4, 6$ and 6). And $2L + 1 < (L + 1)^2$ for $L < 0$.

Considering now, several measurement circles $C^{(\omega_j)}$, $j = 1, 2, \ldots, N_c$, with orientation $\omega_j = (\alpha_j, \beta_j, \gamma_j)$. For each N_c and L, we will have a set of equations of the form (23)–(20):

$$G^{(\omega_j)}_m = \sum_{\substack{\ell=|m| \\ \ell-m \text{ even}}}^{L} y_{\ell,m}\, D^{\ell}_{\bullet,m}(\omega_j)\, F_{\ell,\bullet}\ . \tag{24}$$

They can be written using the double indexes (j and m) and (ℓ and m') for enumerate the arrows and columns of the matrix N_c(2L+1)×(L+1)^2:

$$G = MF \tag{25}$$

where $G = \|G_{j,m}\|\,,\ G_{j,m} = G^{(\omega j)}_m,\ M = \|M_{j,m;\ell,m'}\|\,,\ M_{j,m;\ell,m'} = y_{\ell,m} D^{\ell}_{m',m}(\omega j),\ F = \|F_{\ell,m'}\|\,.$

5. Conclusions

The problem of determining the spherical harmonics of the field $F(\theta,\, \phi)$ over the sphere can be considered as an optimization problem, where there are N_c systems of $2L + 1$ simultaneous equations with $(L + 1)^2$ variables.

If the observations of $F(\theta_n, \phi_n) \Rightarrow F^{(\omega j)}_m \Rightarrow G^{(\omega j)}_m$ are not accurate, we will need to adjust to the harmonic coefficients $F_{\ell,m}$ by minimal square or other algorithm.

Acknowledgements

This work is partially supported by CONACyT, Mexico, under grants 45667 and J34700-T.

REFERENCES

1. Sánchez-Mondragón, J., M. Tecpoyotl-Torres, J. A. Andrade-Lucio, M. Torres-Cisneros, A. Dávila-Alvarez, and M. Carpio-Valadez, "Data fitting on a spherical shell," *Proceedings of SPIE*, Vol. 5181, 51–55, Paper 6, September 2003.
2. Wolf, K. B., Integral Transforms in Science and Engineering, Plenum Publ. Corp., New York, 1979.